Nano Research 2015, 8(12): 4048–4060
DOI 10.1007/s12274-015-0906-8
Research Article
ISSN 1998-0124
CN 11-5974/O4

Complete thermoelectric benchmarking of individual InSb nanowires using combined micro-Raman and electric transport analysis

Sara Yazji[1,2], Eric A. Hoffman[1,2], Daniele Ercolani[3], Francesco Rossella[3], Alessandro Pitanti[3], Alessandro Cavalli[1], Stefano Roddaro[3], Gerhard Abstreiter[1,2], Lucia Sorba[3], and Ilaria Zardo[1,4] (✉)

[1] *Walter Schottky Institut & Physik Department, Technische Universität München, Garching D-85748, Germany*
[2] *Institute for Advanced Study, Technische Universität München, Garching D-85748, Germany*
[3] *NEST, Istituto Nanoscienze-CNR and Scuola Normale Superiore, Pisa I-56127, Italy*
[4] *Department of Physics, University of Basel, CH-4056 Basel, Switzerland*

Received: 6 May 2015
Revised: 9 September 2015
Accepted: 28 September 2015

KEYWORDS
thermoelectric,
thermoelectric figure of merit,
Raman spectroscopy,
field-effect transistor measurements,
nanowire,
InSb

ABSTRACT

Nanowires (NWs) are ideal nanostructures for exploring the effects of low dimensionality and thermal conductivity suppression on thermoelectric behavior. However, it is challenging to accurately measure temperature gradients and heat flow in such systems. Here, using a combination of spatially resolved Raman spectroscopy and transport measurements, we determine all the thermoelectric properties of single Se-doped InSb NWs and quantify the figure of merit ZT. The measured laser-induced heating in the NWs and associated electrical response are well described by a 1D heat equation model. Our method allows the determination of the thermal contact resistances at the source and drain electrodes of the NW, which are negligible in our system. The measured thermoelectric parameters of InSb NWs agree well with those obtained based on field-effect transistor Seebeck measurements.

1 Introduction

High-efficiency heat-electricity conversion can have a major impact on energy production and enable new self-powered device applications. The figure of merit $ZT = \sigma S^2 T/\kappa$ (where σ, S, and κ are the electrical conductivity, Seebeck coefficient, and thermal conductivity, respectively) relates the physical properties of a material to its efficiency as a power generator or heat pump. After the predicted enhancement of the ZT value

Address correspondence to ilaria.zardo@unibas.ch

for materials at the nanoscale [1, 2], many materials with ZT > 1 at room temperature have been discovered [3, 4]; however, a competitive material with ZT > 3 has not yet been developed. A ZT value of ~3 or higher is required for thermoelectric devices to be considered an efficient alternative to mechanical heat engines for power generation, waste-heat harvesting, and refrigeration [5, 6]. To the best of our knowledge, the highest ZT value attained is 2.6 at 923 K, which was realized in SnSe single crystals measured along the *b* axis of the room-temperature orthorhombic unit cell [7]. To obtain a complete determination of the thermoelectric properties of a material, σ, S, and κ must be measured on the same structure under the same conditions. For nanoscale systems, this requirement is experimentally challenging. For nanowires (NWs), κ is often measured using either suspended SiN_x membranes [8–10] or via local laser heating and Raman spectroscopy [11, 12]. S or the power factor σS^2 can instead be measured using devices with metallic resistive thermometers, designed in several geometries [13–16]. A significant effort has been devoted to engineering measurement platforms that allow a complete determination of the thermoelectric properties of individual NWs. Currently, many measurements on NWs have been performed with suspended resistive thermometers similar to the ones described in Ref. [17], which require complex nanofabrication processes. Furthermore, an open issue is the determination of the thermal contact resistance R^C between the NW and thermometers [18].

In this work, we present a new effective method for the determination of the thermoelectric properties and ZT values of single NWs using a combination of spatially resolved Raman spectroscopy and transport measurements. Our approach reduces the effect of the thermal contact resistances, which have proven to be problematic in alternative architectures [19]. In our case, these values can be directly estimated from measurements and are observed to be smaller than the NW thermal resistance. In addition, the method is in principle fully compatible with the field-effect control of the carrier density in the nanostructure, which has been recently recognized to be critical in the investigation of fundamental properties of nanostructured thermoelectric materials [15]. The temperature gradient ΔT necessary for thermoelectric measurements is provided by an excitation laser, which acts also as a thermometer. Raman spectroscopy is used to determine the local temperature increase along the NW. Transport and Raman measurements, together with a simple 1D heating model, enable the determination of the parameters needed for the calculation of ZT together with an estimate of the thermal contact resistance R^C.

We apply this novel method to individual Se-doped InSb NWs, which are expected to be the most promising candidates for thermoelectric application among III-V semiconductors: InSb NWs with diameters of ~10 nm are for instance expected to exhibit ZT values of ~6 at 300 K [20]. In general, InSb is a narrow-band-gap semiconductor (0.18 eV) with a small effective mass at room temperature and high carrier mobility. The thermoelectric properties of bulk InSb have been widely investigated. κ of bulk InSb has been measured in a broad temperature range from 2 to 773 K [21–27], and a room-temperature κ value of ~17 W/mK was reported [24, 25, 28]. A complete thermoelectric property investigation of intrinsic bulk InSb was performed between 100 and 500 °C, and the average ZT value was 0.42×10^{-3} K^{-1} [22]. More recently, for a Te-doped InSb single crystal, a ZT value of 0.6 was obtained at 637 K [29].

InSb NWs with small diameters (~5 nm) have exhibited properties of a Luttinger liquid in both thermopower [30] and κ [31] studies. Thermopower and electrical measurements on unintentionally n-doped NWs with larger diameters (~43 nm) revealed lower S values but larger σ values than those of pure bulk InSb crystals [32]. A recent study on the phonon dispersion of 54-nm-diameter InSb(111) NWs reported a reduced sound speed compared with the bulk, which was attributed to a 35% reduction of the C_{44} elastic constant, opening new scenarios for the determination of possible causes for the reduction of κ in NWs [33]. The complete ZT of single Sb-enriched n-type InSb NWs was recently measured as a function of growth parameters using a suspended microdevice [34]. A large suppression of κ with respect to bulk InSb was observed (~3 times smaller); however, the measured S was smaller with respect to the value measured for single-crystal InSb [29], resulting in a lower ZT

(between 0.002 and 0.006 at room temperature). Here, we obtained ZT values for Se-doped InSb NWs ranging from 0.014 to 0.025 at room temperature, which are slightly larger than previous findings for Sb-enriched InSb NWs but still lower than those of Te-doped bulk single crystals.

2 Results and discussion

We developed a new method for the investigation of the ZT parameter of nanostructured materials using a combination of spatially resolved Raman spectroscopy and transport measurements. Using this framework, we determined the ZT values of several single Se-doped InSb NWs (see S1 in the Electronic Supplementary Material (ESM)). The measured field-effect electron density was 5×10^{17} electrons/cm^3.

To estimate ZT of a system, we need to determine κ, S, and σ. κ of semiconductor NWs has previously been estimated using laser heating and Raman spectroscopy [11, 12]. By employing a combination of spatially resolved Raman spectroscopy and transport measurements, we were able to measure S and σ using a simple method, which will be discussed in the following text.

The excitation laser employed for Raman spectroscopy is moved along the NW, heating it locally, thus generating the necessary temperature gradient ΔT between the ends of the NW, which is suspended between two metallic stripes that act as heat sinks. In addition, two top contacts are deposited at the NW ends, allowing electrical measurements. At each position of the laser, the Raman spectrum and current–voltage (I–V) characteristic are recorded simultaneously. Using the I–V curves, σ as well as the thermovoltage (i.e., the open-circuit voltage V_{OC}) — and therefore S — can be evaluated. The temperature profile along the NW is determined using Raman spectroscopy based on the linear relation between the shift $\Delta\nu$ of the transverse optical (TO) phonon frequency and the increase in temperature caused by the laser heating [35, 36]. Scans along the NWs are performed for several laser powers, i.e., several temperature profiles are measured.

A sketch of the device employed for our measurements is presented in Fig. 1.

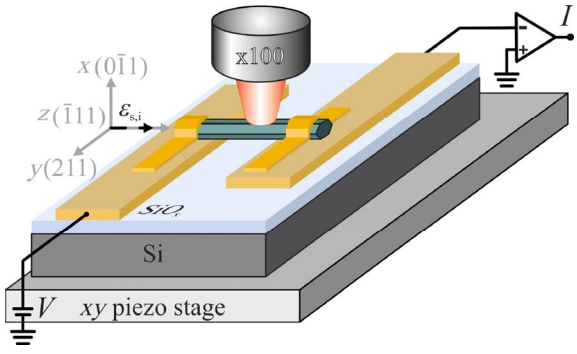

Figure 1 Schematic of the device and scattering geometry used for Raman spectroscopy. The InSb NW is suspended between two gold stripes evaporated on a SiO_2/Si substrate and clamped with two top contacts. A voltage is applied at one end of the NW, and the current is measured through a low-noise current amplifier. The Raman scattering configuration is also shown together with the NW geometry. The entire device is located on a *xy* piezo stage.

Table 1 lists the geometrical characteristics of the NWs investigated using the combined Raman spectroscopy and electrical measurement method. $L_{S,D}$ represents the length of the part of the InSb NW between the source and drain contact, and $L_{thermal}$ represents the length of the suspended part of the NW over the separation between the lower gold stripes. Both lengths are shown in Fig. 2(a). Note that the investigated NW diameter range is far larger than the theoretical one for which a significant improvement of ZT is expected [20]. However, the method described in the present manuscript can be easily applied to thinner NWs because it involves standard NW-based device fabrication processes.

The results obtained using the combined Raman and open-circuit Seebeck measurements were also

Table 1 Geometrical parameters of the investigated Se-doped InSb NWs as estimated from SEM images

Nanowire	Diameter (nm)	$L_{S,D}$ (μm)[a]	$L_{thermal}$ (μm)[b]
A	145	2.200	1.560
B	150	2.240	1.880
C	150	2.340	1.870
D	195	2.410	1.940

[a] $L_{S,D}$ indicated the part of the InSb NW between source and drain contact.

[b] $L_{thermal}$ is the suspended part of the NW over the separation between the lower gold stripes. Both lengths are shown in Fig. 2 (a).

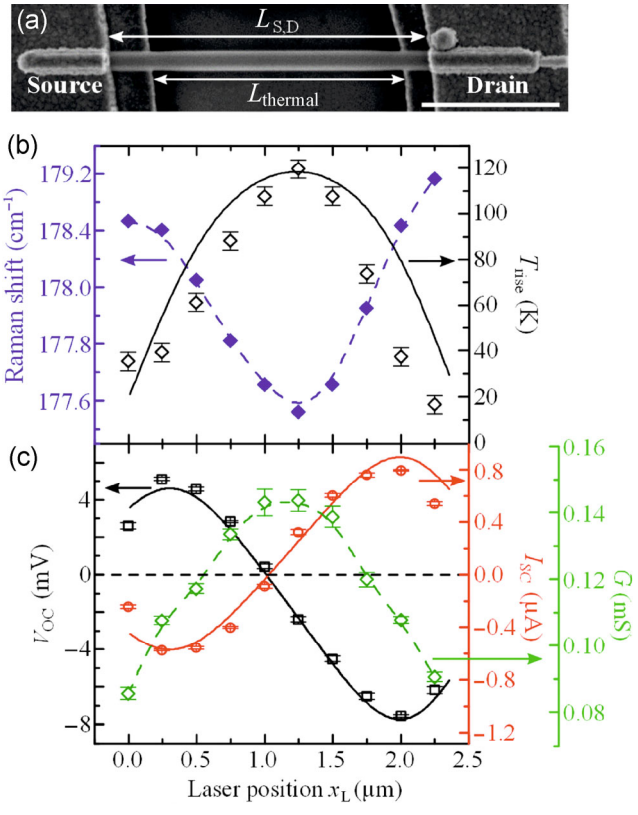

Figure 2 (a) SEM image of one of the investigated Se-doped NWs, with a 150-nm diameter (device C). The NW is suspended between two gold contacts; the two top contacts are visible. $L_{S,D}$ and $L_{thermal}$ are indicated with arrows. The scale bar is 1 μm. (b) Shift of the TO frequency (filled blue diamonds) and local temperature increase (open black diamonds) as a function of the laser position along the NW for 135-μW laser power. (c) V_{OC} (open black squares), I_{SC} (open red circles), and G (open green diamonds) extracted from the I–V characteristic curves measured as a function of the laser position. The I–V measurements were collected simultaneously with the Raman spectra relative to (b). The solid lines are fits of the 1D heating model to the experimental data, and the dashed lines are guides to the eyes.

compared with measurements based on NW field-effect transistors [15]. As discussed further in the following text, these results were particularly useful in assessing the effect of the laser excitation on the thermoelectric response of the NWs. Thus, we fabricated devices implementing a buried heating scheme that allows driving of both a large thermal bias (up to temperature gradients of ~8 K/μm along the NW) and a strong field-effect modulation of electrical conductance on the nanostructure.

With respect to the previous method, this approach suffers from the fact that it does not allow the estimation of the thermal conductance. However, this technique allows the precise mapping of the evolution of S as a function of the gate-controlled σ in the desired temperature range.

2.1 Laser heating and Raman spectroscopy

The combination of laser heating and Raman spectroscopy has already proven to be effective for the determination of κ for NWs [11, 12]. The measurement principle is based on the determination of the local temperature from the shift of the phonon frequencies registered via Raman spectroscopy. The excitation laser itself produces a local increase in temperature, which reflects the creation of a temperature gradient ΔT between the ends of the NW. ΔT is evaluated by fitting the temperature profile with a 1D heat equation, which includes laser heating. We observe a difference in the magnitude of ΔT at the NW ends, which we attribute to a difference in the thermal contact resistances.

We measured the Raman spectra of Se-doped InSb NWs in backscattering configuration and in the geometry illustrated in Fig. 1. The excitation polarization ε_i and detection polarization ε_s were selected parallel to the NW axis z, corresponding to the [$\bar{1}$11] direction. In this geometry, the Raman spectra present the TO at ~179 cm^{-1}, which is the allowed mode from the selection rules, and the forbidden longitudinal optical (LO) mode at 210 cm^{-1} with lower intensity [37]. The shift $\Delta\nu$ of the TO mode caused by laser heating was used to determine the local temperature increase as a function of the laser position x_L. We assumed the same linear coefficient between $\Delta\nu$ and the local temperature rise (with respect to ambient temperature) T_{rise} measured for bulk InSb, i.e., $\Delta\nu/T_{rise}$ = –0.016 cm^{-1}/K [35] in analogy to the experimental observation for Si NWs [38]. Furthermore, for the NW diameters investigated here, we can reasonably assume the bulk relation. However, when using the shift of the optical phonons for the determination of the local temperature increase, particular care must be taken in excluding possible additional shifts not caused by laser heating. For example, depending on the doping level, optical phonon modes could be superimposed with phonon–plasmon modes. In our experiments, this phenomenon can be excluded because a low doping

level was adopted [39]. Alternatively, laser irradiation causes local lattice expansion, with a possible consequent strain distribution in the surroundings [40, 41], which appears as an additional shift of the phonon mode. In this respect, we believe that the strain can be neglected under the experimental conditions used, i.e., continuous-wave laser with relatively low laser power. Indeed, a shorter pulsed laser typically induces a much stronger stress wave [40]. Furthermore, a strain distribution broadens the full-width at half-maximum (FWHM) of the phonon lines, whereas we measured FWHM values comparable to the temperature-dependent ones reported for bulk InSb [36]. Nevertheless, we cannot exclude the presence of a homogenous strain at the point of the excitation source. A typical temperature profile is presented in Fig. 2(b) (open black diamonds) for the NW shown in the scanning electron microscopy (SEM) image in Fig. 2(a) at a fixed laser power (135 μW, corresponding to a power density of 24 kW/cm^2) together with the spatially resolved Raman shifts (filled blue diamonds).

The spectra were collected every 250 nm along the NW. We collected two spectra (180 s of integration per spectrum) for each laser position, which were then averaged. The errors on the temperatures were calculated by propagating the error of the Raman shifts, which were estimated as the maximum error on the Lorentzian fit to the Raman spectra, 0.05 cm^{-1}.

Note that the temperature deduced by Raman spectroscopy is associated with the thermal vibrations of the crystal lattice (lattice temperature). At room temperature, phonons and electrons are well coupled. On the time scale of our measurements, the two systems are in thermal equilibrium, and Raman spectroscopy can be used as a valid electron thermometer.

2.2 Measurements, 1D heating model, and data analysis

The novelty of the measurement technique developed in this work with respect to Ref. [12] is that this approach allows the determination of all the thermoelectric parameters necessary to quantify ZT of an individual NW. Thus far, this possibility has only been demonstrated using architectures based on suspended micro-heater membranes [17], which are technically more challenging and are affected by critical issues in terms of thermal contact resistances [42].

To assess $S = V_{th}/\Delta T$, we need to measure the thermovoltage V_{th} of our system. One possible approach is to directly measure V_{OC} at the NW ends using a high-impedance voltage amplifier while heating the NW with the laser. However, we would not be able to obtain simultaneous information on the changes of σ. We therefore decided to extract V_{OC} from I–V characteristics recorded when varying the position of the laser on the NW. Therefore, we applied an external bias V and recorded I using a low-noise current amplifier. The applied bias was always maintained below 10 mV to avoid additional Joule heating (see S2 for details in the ESM). Without applying a thermal gradient (laser off), for good ohmic contacts, we expect $V\ (I = 0) = 0$. When the laser is on, $\Delta T \neq 0$, and the open circuit thermovoltage appears as well as the short-circuit thermocurrent I_{SC}. From the linear fit to the I–V curves, we can extract V_{OC}, I_{SC}, and the conductance G as a function of the laser position along the NW. At every laser position, we averaged six I–V curves. As an example, the position-dependent I–V curves and Raman spectra relative to Fig. 2 are presented in Fig. S2 (in the ESM). For comparison, we plot the spatially resolved thermovoltages measured both from the I–V curves and with open-circuit conditions in Fig. S3 (in the ESM). In Fig. 2(c), the typical trends of V_{OC}, I_{SC}, and G are shown for one of the Se-doped InSb NW (C) at a fixed laser power. The laser position was varied by moving from the source to the drain contact along the same NW shown in Fig. 2(a), simultaneously recording the Raman spectra from which the temperature profile in Fig. 2(b) was extracted. V_{OC} (I_{SC}) first shows an increase (decrease) then a decrease (increase) as a function of laser position, approaching zero approximately when the local temperature increases reaches the maximum and changing sign moving along the NW. This behavior is exactly in agreement with our expectations: The temperature difference at the contacts, ΔT, is higher when the laser is close to one of the contacts and goes to zero in the middle of the NW (where the local temperature rise is maximum), reversing its sign throughout the other contact. The local temperature profile generated from the laser heating is also reflected in the behavior of G, has

minima at the NW ends (lowest temperature) and a maximum approximately at the NW center (highest temperature). Similar behavior for σ with temperature was observed in independent electrical measurements (see Fig. S4 in the ESM).

Temperature data obtained using Raman spectroscopy together with V_{OC} and I_{SC} data were analyzed using a 1D heating model including a Gaussian heating source, as described in the following text.

Because the electrical contacts have much larger mass and κ than the NW, we treat the contacts as ideal heat sinks that remain at room temperature T_{RT}. The NW temperature, T_{NW}, increases under illumination by the Raman excitation laser positioned at x_L. The laser Gaussian beam profile dissipates its power non-uniformly along the NW, generating a local temperature increase $T(x) = T_{NW}(x) - T_{RT}$. At the same time, heat is dissipated by convection from the NW into the surrounding atmosphere at a rate $\kappa_{air}T(x)$, where κ_{air} is the thermal conductance to air per unit length. Altogether, the 1D heat equation including laser heating and convective cooling is

$$\kappa A\frac{\mathrm{d}^2T(x)}{\mathrm{d}x^2}=\kappa_{air}T(x)-\frac{P_{abs}}{w}\sqrt{\frac{2}{\pi}}\exp\left[-\frac{2(x-x_L)^2}{w^2}\right] \quad (1)$$

where the rightmost term describes the Gaussian laser beam profile centered at x_L with a beam waist w. The Gaussian is normalized such that the total integrated power is $P_{abs} = aP$, where a is the NW absorption coefficient and P is the laser power. A is the cross-sectional area of the NW.

This second-order differential equation requires two boundary conditions that are related to the contact resistances at the source/drain, as discussed in S5 (in the ESM). The laser beam waist is calculated from the measured FWHM, A is calculated from the measured diameters, and the absorbed power P_{abs} is estimated based on *ab initio* finite difference simulations perormed using MEEP software [12, 43]. In Figs. 2(b) and 2(c), the solid lines represent examples of the fit to the experimental data obtained for one NW using a global fit procedure, namely using the same parameters for the entire data set and changing only the laser power. The agreement between the data and the model is quite good.

From the fitting of the Raman temperature increase with the 1D heat equation, the ΔT values were calculated (see S5 in the ESM), and therefore, we could estimate S. The experimental data were also analyzed via an individual fitting procedure, which provided consistent results (see Fig. S6 in the ESM). More details about the fitting procedures are reported in S5 (in the ESM).

In Fig. 3 we present the obtained σ (panel (a)), S (panel (b)), κ (panel (c)), and $R^C_{S,D}$ (panel (d)) values for the investigated Se-doped InSb NWs. Each NW is indicated with a different symbol. In panel (a), the filled symbols represent the maximum electrical conductivities extrapolated from the power dependence of σ (σ_{max}), which were calculated from the position-dependent measurements (see Fig. S7 in the ESM for details). The half-filled symbols represent the dark electrical conductivities measured in the absence of laser excitation. The dashed line represents the σ value measured for Te-doped InSb bulk single crystal [29]. The shaded grey area represents the range of electrical conductivities measured for Sb-doped InSb NWs in Ref. [34]. The values of σ_{max} are similar to previous measurements for Sb-enriched NWs [34]. Note that the difference between σ_{max} and the dark electrical conductivities can possibly be explained by an effective annealing provided by the laser, which increases σ. Indeed, measurements performed after laser illumination with the laser off (data not shown) exhibit a persistent increased σ with respect to that obtained before laser exposure. We observe negative S values, as expected for n-type semiconductors. The absolute value of S of the Se-doped InSb NWs is generally larger than that reported thus far for Sb-enriched InSb NWs [34] but, on average, lower than that measured for bulk Te-doped InSb [29].

The κ values (Fig. 3(c)) are comparable to the intrinsic InSb bulk value [22] and therefore larger than κ measured for InSb NWs in Ref. [34]. This finding could be due to the clean crystalline structure of the investigated NWs together with the fact that in the investigated NW diameter range, a strong effect of boundary scattering is not expected because the phonon mean free path at 300 K is ~84 nm [44]. An evaluation of the diameter dependence of κ is presented in S6 (in the ESM). The fitted value for κ_{air} ranges from 0.09 to 0.18 W/mK (data not shown) and is, therefore, much smaller than the NW κ values.

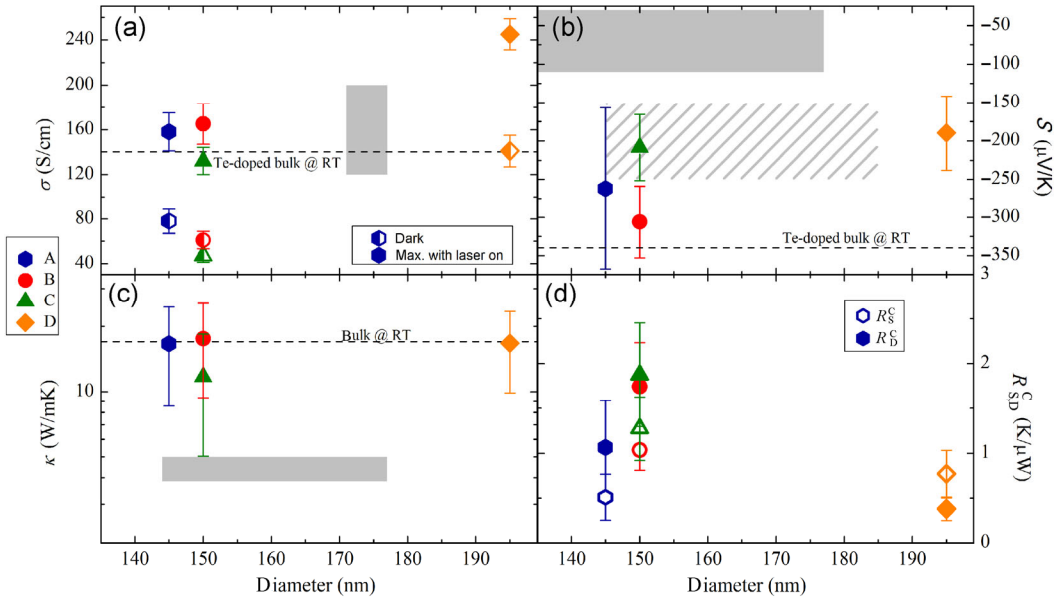

Figure 3 (a) σ of investigated single Se-doped InSb NWs plotted as a function of their diameter. Filled symbols indicate the maximum electrical conductivity extrapolated from the power dependence of σ (σ_{max}), which were calculated from the position-dependent measurements. The half-filled symbols represent the dark electrical conductivities derived from transport measurements. (b) S of the different investigated Se-doped InSb NWs plotted as a function of their diameter. The patterned grey area represents the results obtained using field-effect transistor measurements on NWs of the same growth batch. (c) κ of the different investigated Se-doped InSb NWs plotted as a function of their diameter. (d) The thermal contact resistances for the source (S, filled symbols) and drain (D, empty symbols) as a function of the NW diameter. The values of the different parameters obtained from the same NW are always represented with the same symbol (indicated in the legend). The bulk values of the different parameters are marked as dashed lines for Te-doped single crystal in (a) and (b) [29] and intrinsic bulk in (c) [22]. The range of values obtained for NWs in Ref. [34] are marked as shaded grey areas.

In Fig. 3(d), we present the values calculated from the fitting for the thermal contact resistances at the source and drain, $R^C_{S,D}$. For each NW, we obtain $R^C_S \neq R^C_D$, which explains the asymmetric shape of the Raman temperature profile (see Fig. 2(b)). It is important to note that the NW thermal resistances are ~3 to 40 times larger than the contact thermal resistances, which thus have a minor effect.

More interestingly, the obtained values are ~2 orders of magnitude lower than the measured thermal contact resistances for similar nanostructures on SiN_x membranes, given by point contacts [19]. This result is clearly an important advantage of the method described here, and the large difference is likely due to the more standard and reliable contacting procedures that can be used in our method. The top contacts are prepared using standard lithography, chemical passivation, and selection of the most suitable metal for contacts. In contrast, focused ion beam or electron beam induced deposition (as for membrane devices) restricts the number of metallic contact materials and permits a much more limited control of the interfaces. Therefore, our method provides much better electrical and thermal contacts with respect to the membrane devices.

As discussed in the next section, because the NWs are subject to focused laser excitation, it is important to assess the effect of photo-excited carriers in the described measurement procedure. To this end, we also performed a measurement of σ and S using all-electrical field-effect measurements on the same Se-doped InSb NW as-grown sample investigated using the combined Raman-transport method.

2.3 S and σ determined by field-effect transistor measurements

Because the excitation laser has energy far above the InSb bandgap, one issue that must be considered is the presence of other possible mechanisms that can generate current in semiconductors exposed to illumination.

Spatially resolved photocurrent measurements have been extensively used to investigate carrier transport in NWs, nanotubes, and thin films [45–54]. In addition to the thermoelectric effect, light exposure can generate a built-in electric field responsible for electron–hole separation, which can diffuse or drift to the electric contacts. Recently, electro-thermodynamic modeling of semiconductor NWs under local injection of non-equilibrium carriers has revealed the interplay of the different effects and been used to predict photocurrent profiles for different types of electrical contacts [55]. Time-resolved scanning photocurrent measurements on GaAs and InAs NWs, carbon nanotubes, and graphene have been used to resolve the different temporal contributions to the photocurrent at the picosecond time scale [48, 49, 52, 53]. To understand the possible role of photo-excited charge carriers, independent field-effect transistor measurements of σ and S of individual Se-doped InSb NWs were performed, and the findings were consistent with the results obtained from the combined Raman spectroscopy and transport measurements. This finding provides strong evidence that, even if present, the photovoltaic effect in our measurements is negligible with respect to thermal effects. Furthermore, the temperature dependence of σ as measured from all-electrical measurements (shown in Fig. S4 in the ESM) is comparable to the behavior observed using combined Raman and electrical measurements (Fig. 2(c)), indicating that the sample response is dominated by thermal effects.

Figure 4(a) shows one of the NW field-effect transistor (FET) devices. Se-doped InSb NWs from the same growth batch used for Raman measurements were drop-casted over a SiO_2/Si substrate, and source and drain electrodes were fabricated at a relative distance of 1.1 μm. The multicontact arrangement visible in Fig. 4(a) allows the electrodes to operate both as electrical leads and resistive thermometers, sampling temperatures T_S and T_D at the two ends of the FET and the thermal bias $\Delta T = T_D - T_S$. Operation details and performance of the heating scheme, together with precise information on the measurement procedure, have been presented elsewhere [15, 16]. The direct measurement of T_S and T_D, together with the large ΔT attainable, allow us to determine the precise

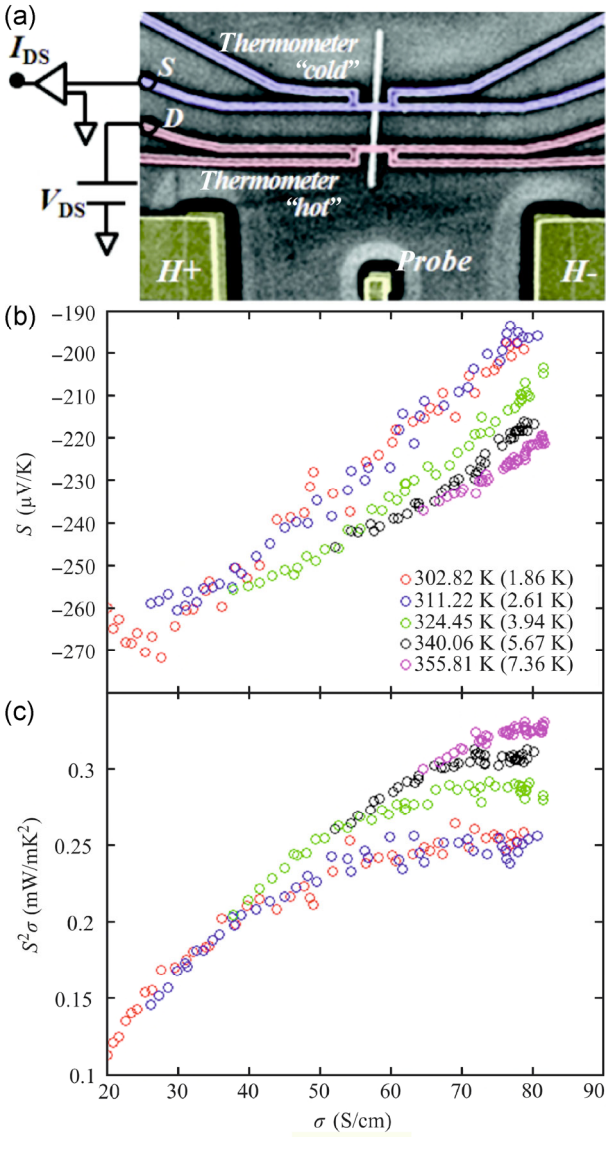

Figure 4 Field-effect Seebeck measurements of individual Se-doped InSb NWs. (a) SEM image of one of the investigated devices. The NW is deposited onto a 300-nm-thick SiO_2 layer grown on top of an n-doped bulk Si substrate, which acts as a back-gate. A buried heater (H^+, H^-) is adopted to induce temperature gradients up to 8 K/μm along the NW axis. Four-terminal Ti/Au electrodes are fabricated at the hot and cold sides of the nanostructure, allowing the AC electrical detection of the temperature difference established between the NW ends and, simultaneously, the DC measurement of the I–V characteristic. The measurement set-up, whose DC part is sketched in the overlay, allows the field-effect control of the resistance R and S. (b) S vs. σ at various temperatures above 300 K. The corresponding temperature differences between the hot and cold end of the NW are reported in brackets. The S values are extracted by the measurement of R and V_{th} for applied back-gate voltages in the range (0, +10 V). (c) The power factor $S^2\sigma$ as a function of σ at various temperatures.

mapping of $S(\sigma,T)$ in the explored temperature range for ΔT ranging from a minimum of ≈0.6 K to a maximum of ≈8.5 K. In Fig. 4(b), we present the S vs. σ curves obtained for five different temperatures above 300 K. The device was thermalized at a temperature of 295 K; then, the local heater was voltage biased to establish the temperature difference indicated in parenthesis in Fig. 4(b) along the NW. S exhibits a monotonic dependence on T for every given value of σ, and the T-dependence of S is linear to a first approximation (although this behavior is more apparent in the S/T vs. σ curves presented in Fig. S11 in the ESM). The corresponding power factor $S^2\sigma$ is plotted as a function of σ in Fig. 4(c).

We highlight that the results obtained using the two different methods correspond well. In both cases, we measured individual Se-doped InSb NWs with diameters of approximately 180 nm from the same growth batch. From the comparison of the data reported in Fig. 3, 4(b), and 4(c), the emerging scenario is that NWs exhibit S values in the range 150–250 μV/K for temperatures above 300 K, and the power factor $S^2\sigma$ exceeds 0.3 mW/(mK^2) with $\sigma > 80$ S/cm.

As an additional assessment of the effect of photo-excitation effects, we also aimed to separate the temporal contribution of the thermocurrent and photocurrent using frequency-dependent measurements by modulating the laser with an optical chopper. The chopper-frequency-dependent measurements are presented in Fig. S13 (in the ESM). We observed a significant variation of the measured photocurrent starting from ~3 kHz up to ~6 kHz, depending on the laser position along the NW. This finding indicates that the main contribution to the photocurrent is due to a mechanism occurring on the time scale of ~300 μs. Because the photocurrent is expected to have a shorter time scale than the thermal mechanism [51], we believe that the measured current is driven by thermal effects.

Finally, in S9 (in the ESM), we present an estimation of the photo- and thermally driven contributions to σ, which also points toward a prevalent thermal effect.

2.4 ZT analysis

From the fitting of the electrical data and temperature profiles, we can estimate κ and S of our Se-doped InSb NWs. These two quantities together with σ measured from the I–V characteristic curves provide ZT. We extracted the ZT value at zero laser power by extrapolating from the power dependence of the maximum ZT measured along the NWs. Details of the ZT calculation are presented in S5 (in the ESM).

The obtained results for the investigated NWs are summarized in Fig. 5.

For comparison, we present the ZT value obtained for a Te-doped InSb bulk single crystal at room temperature [29] as the dashed line and the range of values measured for two Sb-doped InSb NWs from Ref. [34] as the shaded grey area in Fig. 5. For Se-doped InSb NWs with diameters between 130 and 195 nm, we obtain ZT values between 0.014 and 0.025 at room temperature. These values are larger than those reported for Sb-enriched InSb NWs with similar diameters [34] and are the highest ever reported for InSb NWs, to the best of our knowledge. In our case, the S values compensate for the smaller suppression of κ with respect to Ref. [34]. We can attribute this enhancement of ZT to a higher electronic mobility with respect to Ref. [34]. The measured S values are however still lower than those reported for single-crystal InSb for similar values of σ [29], which leads to the currently smaller ZT. We attribute this effect to un-optimal doping in the current InSb nanostructures.

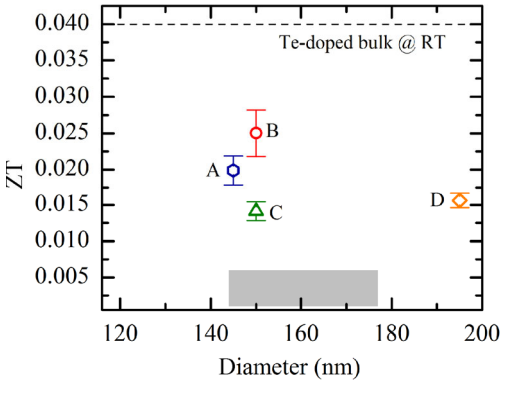

Figure 5 ZT for the Se-doped InSb NWs at zero laser power. Each symbol indicates a different NW. The ZT value for bulk single-crystal Te-doped InSb [29] is marked as a dashed line, and the range of values obtained by NWs from Ref. [34] is marked as the shaded grey area.

3 Conclusion

In conclusion, we presented a new method to obtain a complete benchmark of the thermoelectric properties of individual semiconductor NWs and, in particular, Se-doped InSb NWs. Combined laser heating, Raman spectroscopy, and simple electrical measurements allowed the determination of the ZT value of the NW together with the estimate of the thermal contact resistances at the NW-source/drain contacts. The temperature and electrical data were well described by a 1D heating model, which included a Gaussian heat source. Comparison with field-effect transistor Seebeck measurements revealed good agreement between the obtained results, confirming the validity of the proposed method. The measured ZT values are, to the best of our knowledge, the best reported values thus far for single InSb NWs.

4 Methods

4.1 Nanowire growth

Au-assisted Se-doped InSb NWs were grown using chemical beam epitaxy on InAs (111)B substrates, with a InSb length of ~4.5 μm and diameters in the range of ~50–200 nm. The morphology, structure, and growth protocol of the NWs are presented in detail in S1 (in the ESM).

4.2 Device fabrication and electronic setup

Several parallel gold stripes with 100-nm thickness (10/90 nm of Ti/Au), 2-μm width, and ~2-μm separation were fabricated using optical lithography and metal evaporation on a SiO_2/Si substrate. The InSb NWs were dropcasted on the device, and the wires suspended between two gold stripes were identified using optical imaging. Subsequently, the top contacts were fabricated using electron beam lithography and evaporation of 10/120 nm of Ti/Au. The gold stripes were connected to the electronic setup. The bias was supplied using a DC voltage source, and the current was measured using a low-noise current preamplifier.

4.3 Raman setup

We used the 676.4 nm line (E_L = 1.83 eV) of a tunable Ar^+–Kr^+ laser, focused through a 100× objective with 0.95 numerical aperture, both as the excitation energy for Raman spectroscopy and as a local heater of the NW. The Gaussian spot size of the laser has a FWHM of ~840 nm. For each NW, we selected the laser power to avoid local Sb segregation and structural modification of the NW (see S10 in the ESM) [36, 56]. The Raman spectra were collected using an XY Dilor triple spectrometer equipped with a Si multichannel charged couple detector, with a resolution of ~1 cm^{-1}. The device was placed on a *xy* piezo stage with a precision of 10 nm, which allowed spatially resolved measurements.

4.4 Field-effect transistor measurements

We addressed the thermoelectric response of the NWs for over 40 temperature values between 86 and 360 K (see S7 in the ESM for the full dataset presentation and analysis). Large thermovoltage values in excess of 1 mV were induced in devices comprising a single InSb NW as the active element, and these values were modulated by a field effect. From the back-gate dependence of the conductance, we extracted the standard field-effect electron mobility $\mu_{e,FE}$ value. However, this value is known to be underestimated because it is strongly affected by surface states and gate hysteresis effects. To bypass this issue, we provided an independent estimate of the "Seebeck" electron mobility $\mu_{e,S}$ based on the dependence of the S vs. σ curves on electron scattering times (see S11 in the ESM) [15].

Acknowledgements

We thank M. Bichler and H. Riedl for excellent experimental help. We acknowledge financial support by the Deutsche Forschungsgemeinschaft via the Excellence Cluster "Nanosytems Initiative Munich" and the TUM Institute for Advanced Study. F. R. acknowledges financial support from the Italian MIUR through the FIRB - "Futuro in Ricerca" project BFR13NEA4 "UltraNano".

Electronic Supplementary Material: Supplementary material (description of nanowire synthesis, example of *I*–*V* curves and Raman spectra, comparison with

short circuit measurements, temperature dependence of electrical conductivity, details on fitting procedure and on figure of merit evaluation, thermal conductivity diameter dependence, full field-effect transistor measurements, frequency dependent thermocurrent measurements, photo-and thermally driven electrical conductivity, laser induced Sb precipitation, and mobility calculation) is available in the online version of this article at http://dx.doi.org/10.1007/s12274-015-0906-8.

References

[1] Hicks, L. D.; Dresselhaus, M. S. Effect of quantum-well structures on the thermoelectric figure of merit. *Phys. Rev. B* **1993**, *47*, 12727–12731.

[2] Hicks, L. D.; Dresselhaus, M. S. Thermoelectric figure of merit of a one-dimensional conductor. *Phys. Rev. B* **1993**, *47*, 16631–16634.

[3] Majumdar, A. Thermoelectricity in semiconductor nanostructures. *Science* **2004**, *303*, 777–778.

[4] Heremans, J. P.; Dresselhaus, M. S.; Bell, L. E.; Morelli, D. T. When thermoelectrics reached the nanoscale. *Nat. Nanotechnol.* **2013**, *8*, 471–473.

[5] Bell, L. E. Cooling, heating, generating power, and recovering waste heat with thermoelectric systems. *Science* **2008**, *321*, 1457–1461.

[6] DiSalvo, F. J. Thermoelectric cooling and power generation. *Science* **1999**, *285*, 703–706.

[7] Zhao, L.-D.; Lo, S.-H.; Zhang, Y. S.; Sun, H.; Tan, G. J.; Uher, C.; Wolverton, C.; Dravid V. P.; Kanatzidis M. G. Ultralow thermal conductivity and high thermoelectric figure of merit in SnSe crystals. *Nature* **2014**, *508*, 373–377.

[8] Roh, J. W.; Jang S. Y.; Kang, J.; Lee, S.; Noh, J.-S.; Kim, W.; Park, J.; Lee, W. Size-dependent thermal conductivity of individual single-crystalline PbTe nanowires. *Appl. Phys. Lett.* **2010**, *96*, 103101.

[9] Li, D. Y.; Wu, Y. Y.; Kim, P.; Shi, L.; Yang, P. D.; Majumdar, A. Thermal conductivity of individual silicon nanowires. *Appl. Phys. Lett.* **2003**, *83*, 2934–2936.

[10] Zhou, F.; Moore, A. L.; Bolinsson, J.; Persson, A.; Fröberg, L.; Pettes, M. T.; Kong, H. J.; Rabenberg, L.; Caroff, P.; Stewart, D. A. et al. Thermal conductivity of indium arsenide nanowires with wurtzite and zinc blende phases. *Phys. Rev. B* **2011**, *83*, 205416.

[11] Doerk, G. S.; Carraro, C.; Maboudian, R. Single nanowire thermal conductivity measurements by Raman thermography. *ACS Nano* **2010**, *4*, 4908–4914.

[12] Soini, M.; Zardo, I.; Uccelli, E.; Funk, S.; Koblmüller, G.; Fontcuberta i Morral, A.; Abstreiter, G. Thermal conductivity of GaAs nanowires studied by micro-raman spectroscopy combined with laser heating. *Appl. Phys. Lett.* **2010**, *97*, 263107.

[13] Zhou, F.; Seol, J. H.; Shi, L.; Ye, Q. L.; Scheffler, R. One-dimensional electron transport and thermopower in an individual InSb nanowire. *J. Phys.: Condens. Matter* **2006**, *18*, 9651–9657.

[14] Shapira, E.; Tsukernik, A.; Selzer, Y. Thermopower measurements on individual 30 nm nickel nanowires. *Nanotechnology* **2007**, *18*, 485703.

[15] Roddaro, S.; Ercolani, D.; Safeen, M. A.; Suomalainen, S.; Rossella, F.; Giazotto, F.; Sorba, L.; Beltram, F. Giant thermovoltage in single InAs nanowire field-effect transistors. *Nano Lett.* **2013**, *13*, 3638−3642.

[16] Roddaro, S.; Ercolani, D.; Safeen, M. A.; Rossella, F.; Piazza, V.; Giazotto, F.; Sorba, L.; Beltram, F. Large thermal biasing of individual gated nanostructures. *Nano Res.* **2014**, *7*, 579–587.

[17] Shi, L.; Li, D. Y.; Yu, C.; Jang, W.; Kim, D.; Yao, Z.; Kim, P.; Majumdar, A. Measuring thermal and thermoelectric properties of one-dimensional nanostructures using a microfabricated device. *J. Heat Transfer* **2003**, *125*, 881–888.

[18] Shi, L. Thermal and thermoelectric transport in nanostructures and low-dimensional systems. *Nanosc. Microsc. Therm.* **2012**, *16*, 79–116.

[19] Zhou, F.; Perrson, A.; Samuelson, L.; Linke, H.; Shi, L. Thermal resistance of a nanoscale point contact to an indium arsenide nanowire. *Appl. Phys. Lett.* **2011**, *99*, 063110.

[20] Mingo, N. Thermoelectric figure of merit and maximum power factor in III–V semiconductor nanowires. *Appl. Phys. Lett.* **2004**, *84*, 2652–2654.

[21] Stuckes, A. D. Thermal conductivity of indium antimonide. *Phys. Rev.* **1957**, *107*, 427–428.

[22] Bowers, R.; Ure, R. W. Jr.; Bauerle, J. E.; Cornish, A. J. InAs and InSb as thermoelectric materials. *J. Appl. Phys.* **1959**, *30*, 930–934.

[23] Mielczarek, E. V.; Frederiske, H. P. R. Thermal conductivity of indium antimonide at low temperatures. *Phys. Rev.* **1959**, *115*, 888–891.

[24] Steigmeier, E. Wärmeleitfähigkeit, elektrische leitfähigkeit, Hall-effekt und thermospannung von InSb. *Helv. Phys. Acta.* **1961**, *34*, 1–28.

[25] Holland, M. G. Phonon scattering in semiconductors from thermal conductivity studies. *Phys. Rev.* **1964**, *134*, A471–A480.

[26] Bhandari, C. M.; Verma, G. S. Role of longitudinal and transverse phonons in lattice thermal conductivity of GaAs and InSb. *Phys. Rev.* **1968**, *176*, 1112.

[27] Kosarev, V. V.; Tamarin, P. V.; Shalyt, S. S. Thermal conductivity of indium antimonide at low temperatures. *Phys. Stat. Solidi (b)* **1971**, *44*, 525–530.

[28] Nakwaski, W. Thermal conductivity of binary, ternary, and quaternary III-V compounds. *J. Appl. Phys*. **1988**, *64*, 159–166.

[29] Yamaguchi, S.; Matsumoto, T.; Yamazaki, J.; Kaiwa, N.; Yamamoto, A. Thermoelectric properties and figure of merit of a Te-Doped InSb bulk single crystal. *Appl. Phys. Lett.* **2005**, *87*, 201902.

[30] Vedernikov, M. V.; Uryupin, O. N.; Goltsman, B. M.; Ivanov, Y. V.; Kumzerov, Y. A. Experimental thermopower of quantum wires. *MRS Proc.* **2001**, *691*, DOI: 10.1557/PROC-691-G8.34.

[31] Kumzerov, Y. A.; Smirnov, I. A.; Firsov, Y. A.; Parfen'eva, L. S.; Misiorek, H.; Mucha, J.; Jezowski, A. Thermal conductivity of ultrathin InSb semiconductor nanowires with properties of the luttinger liquid. *Phys. Solid State* **2006**, *48*, 1584–1590.

[32] Seol, J. H.; Moore, A. L.; Saha, S. K.; Zhou, F.; Shi, L.; Ye, Q. L.; Scheffler, R.; Mingo, N.; Yamada, T. Measurement and analysis of thermopower and electrical conductivity of an indium antimonide nanowire from a vapor-liquid-solid method. *J. Appl. Phys.* **2007**, *101*, 023706.

[33] Jurgilaitis, A.; Enquist, H.; Andreasson, B. P.; Persson, A. I. H.; Borg, B. M.; Caroff, P.; Dick, K. A.; Harb, M.; Linke, H.; Nüske, R. et al. Time-resolved X-ray diffraction investigation of the modified phonon dispersion in InSb nanowires. *Nano Lett.* **2014**, *14*, 541–546.

[34] Zhou, F.; Moore, A. L.; Pettes, M. T.; Lee, Y.; Seol, J. H.; Ye, Q. L.; Rabenberg, L.; Shi, L. Effect of growth base pressure on the thermoelectric properties of indium antimonide nanowires. *J. Phys. D: Appl. Phys.* **2010**, *43*, 025406.

[35] Costa, S. C.; Pizani, P. S.; Rino, J. P. Molecular dynamics simulation of dynamical properties of InSb. *Phys. Rev. B* **2003**, *68*, 073204.

[36] Liarokapis, E.; Anastassakis, E. Light scattering of InSb at high temperatures. *Phys. Rev. B* **1984**, *30*, 2270–2272.

[37] Zardo, I.; Conesa-Boj, S.; Peiro, F.; Morante, J. R.; Arbiol, J.; Uccelli, E.; Abstreiter, G.; Fontcuberta i Morral, A. Raman spectroscopy of wurtzite and zinc-blende GaAs nanowires: Polarization dependence, selection rules, and strain effects. *Phys. Rev. B* **2009**, *80*, 245324.

[38] Doerk, G. S.; Carraro, C.; Maboudian, R. Temperature dependence of Raman spectra for individual silicon nanowires. *Phys. Rev. B* **2009**, *80*, 073306.

[39] Pinczuk A.; Burstein, E. Raman scattering from InSb surfaces at photon energies near the E_1 energy gap. *Phys. Rev. Lett.* **1968**, *21*, 1073–1075.

[40] Wang, X.; Xu, X. Thermoelastic wave induced by pulsed laser heating. *Appl. Phys. A* **2001**, *73*, 107–114.

[41] Lo, H. W; Compaan, A. Raman measurements of temperature during cw laser heating of silicon. *J. Appl. Phys*. **1980**, *51*, 1565–1568.

[42] Swinkels, M. Y.; van Delft, M. R.; Oliveira, D. S.; Cavalli, A.; Zardo, I.; van der Heijden, R. W.; Bakkers, E. P. A. M. Diameter dependence of the thermal conductivity of InAs nanowires. *Nanotechnology* **2015**, *26*, 385401.

[43] Oskooi, A. F.; Roundy, D.; Ibanescu, M.; Bermel, P.; Joannopoulos, J. D.; Johnson, S. G. MEEP: A flexible free-software package for electromagnetic simulations by the FDTD method. *Comp. Phys. Commun.* **2010**, *181*, 687–702.

[44] Seol, J. H. Thermal and Thermoelectric Measurements of Silicon Nanoconstrictions, Supported Graphene, and Indium Antimonide Nanowires. Ph. D. Dissertation, University of Texas, TX, USA, 2009.

[45] Pettersson, H.; Trägårdh, J.; Persson, A. I.; Landin, L.; Hessman, D.; Samuelson, L. Infrared photodetectors in heterostructure nanowires. *Nano Lett.* **2006**, *6*, 229–232.

[46] Thunich, S.; Prechtel, L.; Spirkoska, D.; Abstreiter, G.; Fontcuberta i Morral, A.; Holleitner, A. W. Photocurrent and photoconductance properties of a GaAs nanowire. *Appl. Phys. Lett.* **2009**, *95*, 083111.

[47] Varghese, B.; Tamang, R.; Tok, E. S.; Mhaisalkar, S. G.; Sow, C. H. Photothermoelectric effects in localized photocurrent of individual VO_2 nanowires. *J. Phys. Chem. C* **2010**, *114*, 15149–15156.

[48] Prechtel, L.; Padilla, M.; Erhard, N.; Karl, H.; Abstreiter, G.; Fontcuberta i Morral, A.; Holleitner, A. W. Time-resolved photoinduced thermoelectric and transport currents in GaAs nanowires. *Nano Lett.* **2012**, *12*, 2337–2341.

[49] Erhard, N.; Seifert, P.; Prechtel, L; Hertenberger, S.; Karl, H.; Abstreiter, G.; Koblmüller, G.; Holleitner, A. W. Ultrafast photocurrents and THz generation in single InAs-nanowires. *Ann. Phys.* **2013**, *525*, 180–188.

[50] St-Antoine, B. C.; Ménard, D.; Martel, R. Position sensitive photothermoelectric effect in suspended single-walled carbon nanotube films. *Nano Lett.* **2009**, *9*, 3503–3508.

[51] St-Antoine, B. C.; Ménard, D.; Martel, R. Photothermoelectric effects in single-walled carbon nanotube films: Reinterpreting scanning photocurrent experiments. *Nano Res.* **2012**, *5*, 73–81.

[52] Prechtel, L.; Song, L.; Manus, S.; Schuh, D.; Wegscheider,

W.; Holleitner, A. W. Time-resolved picosecond photocurrents in contacted carbon nanotubes. *Nano Lett.* **2011**, *11*, 269–272.

[53] Prechtel, L.; Song, L.; Schuh, D.; Ajayan, P.; Wegscheider, W.; Holleitner, A. W. Time-resolved ultrafast photocurrents and terahertz generation in freely suspended graphene. *Nat. Commun*. **2012**, *3*, 646.

[54] Buscema, M.; Barkelid, M.; Zwiller, V.; van der Zant, H. S. J.; Steele, G. A.; Castellanos-Gomez, A. Large and tunable photothermoelectric effect in single-layer MoS_2. *Nano Lett.* **2013**, *13*, 358–363.

[55] Fu, D. Y.; Zou, J. J.; Wang, K.; Zhang, R.; Yu, D.; Wu, J. Q. Electrothermal dynamics of semiconductor nanowires under local carrier modulation. *Nano Lett*. **2011**, *11*, 3809–3815.

[56] Yazji, S.; Zardo, I.; Soini, M.; Postorino, P.; Fontcuberta i Morral, A.; Abstreiter, G. Local modification of GaAs nanowires induced by laser heating. *Nanotechnology* **2011**, *22*, 325701.